

Modeling bound-to-continuum terahertz quantum cascade lasers: The role of Coulomb interactions

Christian Jirauschek,^{1,2, a)} Alpar Matyas,^{1,2} and Paolo Lugli²

¹⁾*Emmy Noether Research Group “Modeling of Quantum Cascade Devices”, Technische Universität München, D-80333 Munich, Germany*

²⁾*Institute for Nanoelectronics, Technische Universität München, D-80333 Munich, Germany*

(Dated: 25 May 2022, published as J. Appl. Phys. 107, 013104 (2010))

Based on an ensemble Monte Carlo analysis, we show that Coulomb interactions play a dominant role in bound-to-continuum terahertz quantum cascade lasers and thus require careful modeling. Coulomb interactions enter our simulation in the form of space charge effects as well as Coulomb scattering events. By comparison to a full many-subband Coulomb screening model, we show that simplified approaches produce considerable deviations for such structures. Also the spin dependence of electron-electron scattering has to be adequately considered. Moreover, we demonstrate that iterative Schrödinger-Poisson and carrier transport simulations are necessary to correctly account for space charge effects.

PACS numbers: 42.55.Px, 73.63.Hs, 78.70.Gq

I. INTRODUCTION

For terahertz quantum cascade lasers (QCLs), two types of structures play a major role: the resonant-phonon (RP) and the bound-to-continuum (BTC) design. In RP structures, efficient depletion of the lower laser level is achieved by tuning the corresponding transition to the longitudinal-optical (LO) phonon energy (36 meV in GaAs). By contrast, BTC designs are based on minibands, enhancing the influence of Coulomb interactions in two ways. First, the close energetic spacing of the miniband levels favors electron-electron (e-e) over LO phonon scattering in the carrier transport. Also, the large spatial extent of the minibands across many wells, together with the localization of the positively charged donors in typically a single well, leads to considerable conduction band bending due to space charge effects.¹ Thus, a careful modeling of Coulomb interactions is necessary to analyze carrier transport in BTC QCLs, and here specifically the role of Coulomb interactions in such structures. However, e-e scattering is much more computationally demanding than single-electron processes like electron-phonon interactions, hampering its inclusion in quantum mechanical simulations of QCLs beyond the mean-field approximation.² The numerical load is further increased by the large spatial extent of the minibands. Due to its efficiency, the semiclassical ensemble Monte-Carlo (EMC) method is well-suited for investigating BTC structures. However, EMC simulations have up to now typically focused on terahertz RP structures,³⁻⁹ while only few results are available for equivalent BTC or related chirped superlattice designs.^{10,11}

We present an EMC simulation tool optimized for the simulation of terahertz BTC structures. We employ a full many-subband (MS) screening model for electron-electron scattering and include the exchange effect for the parallel-spin collisions. Space charge effects are adequately considered

by performing iterative Schrödinger-Poisson (SP) and carrier transport simulations, yielding so-called self-self-consistent solutions.¹ This tool allows us to properly assess the role of Coulomb interactions for the carrier transport and gain in a typical terahertz BTC design. Widely-used approximations, such as non-iterative simulations, using simplified screening models, or neglecting the spin dependence of e-e scattering, usually work well for RP structures, but can lead to significant deviations for terahertz BTC QCLs, as shown in this paper.

II. METHOD

The simulation tool, consisting of a three-dimensional EMC and an SP solver, allows for a self-consistent analysis of the carrier transport and optical gain in the QCL structure.¹¹ The SP solver yields the subband eigenenergies and wave functions, needed as an input for the semiclassical EMC carrier transport simulation. The obtained electron distribution in the structure gives rise to space charge effects, resulting in conduction band bending and altered subbands. Thus, iterative runs of SP and EMC simulations are necessary to obtain convergence, corresponding to self-self-consistent solutions.¹

All essential scattering mechanisms are accounted for in the carrier transport simulation. Included is elastic electron-impurity (e-i) and interface roughness scattering, as well as inelastic interactions of electrons with acoustic and longitudinal-optical (LO) phonons. Nonequilibrium phonon effects are also taken into account.¹² Being evaluated as a two-electron process, e-e scattering assumes a special role in the EMC simulation and has the highest computational complexity. Its implementation is more closely discussed in Section II B. For all scattering processes, Pauli’s exclusion principle is taken into account.¹³ Periodic boundary conditions are employed, i.e., electrons leaving the device on one side are automatically injected into the equivalent subband on the opposite side.³

Coulomb interactions enter our simulation in the form of space charge effects as well as individual e-e and e-i scatter-

^{a)}Electronic mail: jirauschek@tum.de; <http://www.nano.ei.tum.de/noether>

ing events. As discussed above, space charge effects and e-e scattering play an especially important role in THz BTC structures due to the formation of minibands. Thus, the implementation of these mechanisms will be discussed in detail in the following.

A. Space charge effects

The subband wave functions $\psi_n(z)$ and eigenenergies E_n for the simulated QCL structure are obtained by solving the SP system¹⁴

$$\left(-\frac{\hbar^2}{2}\partial_z\frac{1}{m^*}\partial_z + V - E_n\right)\psi_n = 0, \quad (1a)$$

$$-\varepsilon\partial_z^2\phi - e\left(N - \sum_n n_{2D,n}|\psi_n|^2\right) = 0. \quad (1b)$$

Here, a position independent permittivity ε is assumed. Furthermore, $m^*(z)$ and $N(z)$ are the electron effective mass and doping concentration of the structure, e and \hbar are the elementary charge and the reduced Planck constant, and $n_{2D,n}$ is the electron sheet density of level n . The self-consistent potential is given by $V(z) = V_0(z) - e\phi(z)$, where V_0 is the conduction band profile and ϕ is the electric potential due to the space charge profile. For QCLs, the subband energies and wave functions are typically computed for a single central period of the structure; the subbands in other periods are then obtained by appropriate shifts of the solutions in energy and position. For the first run of the SP solver, a thermal occupation of the subbands according to Fermi-Dirac statistics is assumed.¹⁴ To obtain self-self-consistent solutions, the subband occupations are subsequently extracted from the EMC analysis, which is carried out alternately with the SP simulation until mutual convergence is obtained.

B. Electron-electron scattering

In the EMC simulation, e-e scattering is implemented as a two-electron process.^{15,16} An electron in an initial state $|i\mathbf{k}\rangle$, i.e., subband i and in-plane wave vector \mathbf{k} , scatters to a final state $|j\mathbf{k}'\rangle$, accompanied by a transition of a second electron from a state $|i_0\mathbf{k}_0\rangle$ to $|j_0\mathbf{k}'_0\rangle$. The total scattering rate from $|i\mathbf{k}\rangle$ to a subband j is then obtained by the Fermi golden rule,

$$R_{i\mathbf{k}\rightarrow j} = \frac{m^*}{4\pi\hbar^3 A} \sum_{i_0, j_0, \mathbf{k}_0} f_{i_0}(\mathbf{k}_0) \int_0^{2\pi} d\theta |M_{ii_0jj_0}(Q)|^2, \quad (2)$$

with the electron effective mass m^* , cross section area A and carrier distribution function f_{i_0} in subband i_0 . θ is the angle between $\mathbf{g} = \mathbf{k}_0 - \mathbf{k}$ and $\mathbf{g}' = \mathbf{k}'_0 - \mathbf{k}'$, and $\mathbf{Q} = \mathbf{k} - \mathbf{k}'$ (with $Q = |\mathbf{Q}|$) denotes the exchanged wavevector.

Different approaches with varying degrees of complexity exist to compute the transition matrix element $M_{ii_0jj_0}$ from

the bare Coulomb matrix elements,

$$V_{ii_0jj_0}^b(Q) = \frac{e^2}{2\varepsilon Q} \int_{-\infty}^{\infty} dz \int_{-\infty}^{\infty} dz' [\psi_i(z)\psi_{i_0}(z') \times \psi_j(z)\psi_{j_0}(z') \exp(-Q|z-z'|)]. \quad (3)$$

First, the screened Coulomb matrix elements $V_{ii_0jj_0}^s(Q)$ are obtained from $V_{ii_0jj_0}^b(Q)$ by applying a more or less sophisticated screening model. In the random phase approximation (RPA), they are found by solving the equation system¹⁷

$$V_{ii_0jj_0}^s = V_{ii_0jj_0}^b + \sum_{mn} V_{imjn}^b \Pi_{mn} V_{mi_0nj_0}^s. \quad (4)$$

Here, $\Pi_{mn}(Q)$ is the polarizability tensor, given in the long wavelength limit ($Q \rightarrow 0$) by

$$\Pi_{mn} = \begin{cases} \frac{n_{2D,m} - n_{2D,n}}{E_m - E_n}, & m \neq n, \\ -\frac{m^*}{\pi\hbar^2} f_n(0), & m = n. \end{cases} \quad (5)$$

For collisions of electrons with parallel spin, interference occurs between $V_{ii_0jj_0}^s$ and the 'exchange' matrix element $V_{ii_0j_0j}^s$.¹⁸ Accounting for this exchange effect, the magnitude squared of the transition matrix element $M_{ii_0jj_0}$ is then given by^{16,18}

$$|M_{ii_0jj_0}|^2 = \frac{p_a}{2} \left[|V_{ii_0jj_0}^s(Q^-)|^2 + |V_{ii_0j_0j}^s(Q^+)|^2 \right] + \frac{p_p}{2} |V_{ii_0jj_0}^s(Q^-) - V_{ii_0j_0j}^s(Q^+)|^2, \quad (6)$$

where $p_a = p_p = 1/2$ are the probabilities for antiparallel and parallel spin collisions, respectively, and

$$Q^\pm = \frac{1}{2} \left[2g^2 + g_0^2 \pm 2g(g^2 + g_0^2)^{1/2} \cos\theta \right]^{1/2}, \quad (7)$$

with $g = |\mathbf{g}|$ and $g_0^2 = 4m^*(E_i + E_{i_0} - E_j - E_{j_0})/\hbar^2$.

Commonly, simplified screening models are used to avoid the numerical load associated with solving Eq. (4).^{6,7} Furthermore, often the exchange effect is neglected when calculating $M_{ii_0jj_0}$.¹⁸ As discussed in Section I, e-e scattering plays a particularly significant role in BTC structures. Thus, the validity of such approximations in BTC designs deserves special scrutiny, as shown below.

III. RESULTS AND DISCUSSION

We present simulation results for a 3.5 THz BTC design,¹⁹ demonstrating the importance of Coulomb interactions on the carrier transport and material gain in such structures. In particular, we investigate the validity of neglecting the exchange effect and employing simplified screening models for the evaluation of e-e scattering. Also the importance of self-self-consistent simulations for a proper inclusion of space charge effects is discussed. In our EMC simulation, all scattering mechanisms are evaluated self-consistently. Only interface roughness (IR), whose parameters are hard to measure and

depend critically on the growth conditions, has to be described in terms of a phenomenological model.^{11,20} For the IR mean height and correlation length, we use typical values of $\Delta = 0.12$ nm, $\Gamma = 10$ nm.^{11,21}

A. Space charge effects

In Fig. 1, the simulated conduction band profile and spectral gain of the investigated BTC QCL is shown for a lattice temperature $T_L = 10$ K at the design bias of 2.5 kV/cm, where the maximum gain is obtained in the simulation. Solid lines indicate fully self-self-consistent results; here, the SP and EMC simulations are carried out iteratively until convergence is obtained. Dashed lines indicate the results obtained by solving the SP system once in the beginning assuming a thermal carrier distribution,¹⁴ and then performing a self-consistent EMC simulation, which is a quite common approach.^{3,6,8,9} For comparison, also the conduction band profile and spectral gain is shown as obtained with deactivated Poisson solver (dotted lines), i.e., when no space charge effects are included. In all cases, e-e scattering is evaluated taking into account the exchange effect as well as screening, which is considered in RPA by repeatedly solving Eq. (4) to account for changes in the carrier distribution during the EMC simulation.

The results shown in Fig. 1 indicate that the proper inclusion of space charge effects greatly affects the simulation outcome for the investigated BTC structure. A significant conduction band bending is observed for activated Poisson solver (solid and dashed lines in Fig. 1(a)), changing the sub-band eigenenergies and wave functions. Comparison to experimental data shows that only the simulation results with space charge effects included are in line with experiment. The gain profile obtained with deactivated Poisson solver is exceedingly broad, flat and low, see Fig. 1(b) (dotted curve). The low peak gain of around 9 cm^{-1} at around 4.2 THz is in sharp contrast to the experimentally observed lasing of the structure at 3.5 THz.¹⁹ Also the large gain bandwidth is not in accord with electroluminescence measurements, yielding full width at half maximum (FWHM) widths of clearly below 1 THz.¹⁹ The inclusion of space charge effects leads to a realistic gain profile centered around 3.5 THz in agreement with experiment. The FWHM widths of 0.65 THz (solid curve) and 0.66 THz (dashed curve) agree reasonably well with the experimental value of 0.85 THz at 10 K, extracted from electroluminescence measurements.¹⁹ Still, the two gain profiles are somewhat different, with peak gain values of 24.2 cm^{-1} for the self-self-consistent and 21.2 cm^{-1} for the non-iterative approach. This illustrates the importance of self-self-consistent simulations for terahertz BTC designs, where space charge effects tend to play a more pronounced role than in equivalent RP structures.

B. Exchange effect

There are two common approaches to implement e-e scattering without explicitly considering the spin dependence.

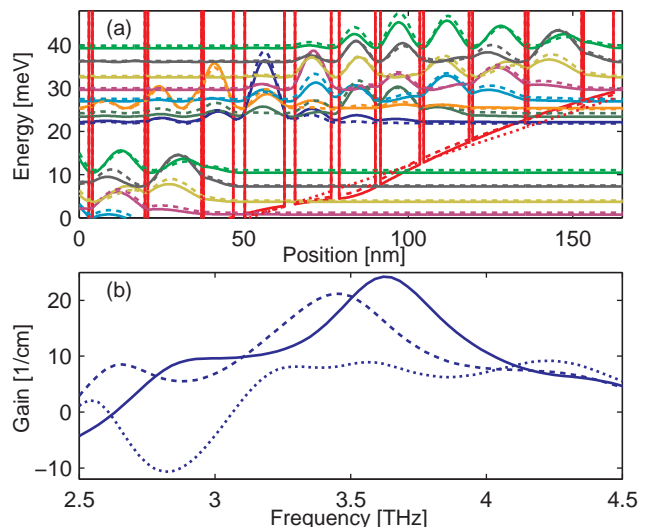


FIG. 1. (Color online) (a) Conduction band profile and probability densities, as obtained for thermally occupied subbands (dashed lines) and by a self-self-consistent simulation (solid lines). For comparison, also the conduction band profile without space charge effects included is displayed (dotted line). (b) Simulated spectral gain versus frequency for the cases shown above.

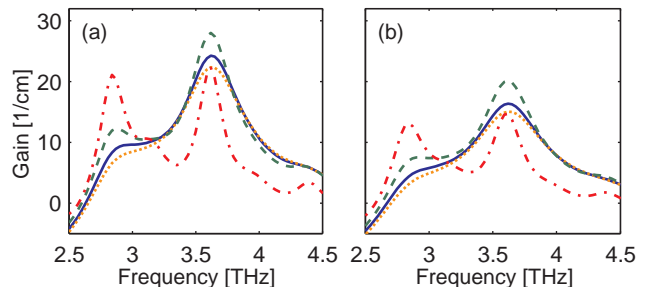


FIG. 2. (Color online) Simulated spectral gain vs frequency, as obtained by fully taking into account (solid curves) and ignoring the exchange effect (dotted curves), and by ignoring parallel spin collisions (dashed curves). For comparison, the result obtained with no e-e scattering is also shown (dash-dotted curves). (a) $T_L = 10$ K; (b) $T_L = 90$ K.

One method, which tends to overestimate the exchange effect, is to completely neglect the parallel spin collisions,^{15,18} implying $p_a = 1/2$, $p_p = 0$ in Eq. (6). Another common approach is to ignore the spin dependence. Parallel spin collisions are then treated the same way as antiparallel spin contributions,¹⁸ which corresponds to $p_a = 1$, $p_p = 0$ in Eq. (6). In moderately doped RP structures at elevated temperatures, where the carrier transport is dominated by LO phonon scattering, the contribution of the exchange effect is usually negligible. In BTC designs, based on minibands with closely spaced energy levels, e-e scattering plays a more pronounced role.¹¹

Figure 2 contains the self-self-consistently simulated gain spectra at $T_L = 10$ K and $T_L = 90$ K, taking into account screening in the RPA. Results are shown for $p_a = p_p = 1/2$

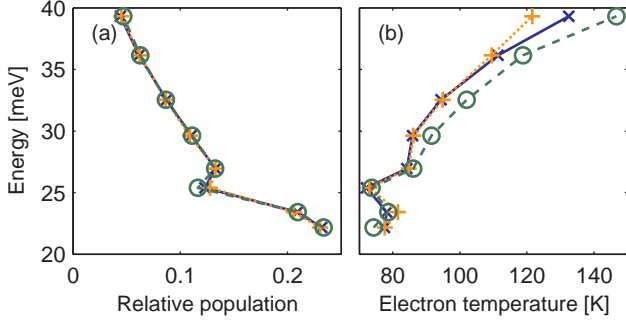


FIG. 3. (Color online) Simulation results for (a) relative subband occupations and (b) subband temperatures, as obtained by fully taking into account (x-marks, solid curves) and ignoring the exchange effect (plus signs, dotted curves), and by ignoring parallel spin collisions (circles, dashed curves). The lines are guide to the eye.

(solid curve), $p_a = 1, p_p = 0$ (dotted curve), $p_a = 1/2, p_p = 0$ (dashed curve), and $p_a = p_p = 0$ (dash-dotted curve). The last case, which corresponds to completely neglecting e-e scattering in the simulation, yields two narrow gain spikes around 2.8 and 3.6 THz, largely deviating from the experimental electroluminescence measurements.¹⁹ This illustrates the importance of e-e scattering for such structures. As discussed in Section III A, for $T_L = 10$ K the full simulation with exchange effect included yields a realistic gain profile, see solid curve in Fig. 2(a). Ignoring exchange (dotted curve) leads to an overestimation of the scattering, resulting in a peak gain reduction by 8%, and an increase of the FWHM gain width by 11%. On the other hand, completely neglecting parallel spin collisions (dashed curve) leads to a gain width reduction of 24%, and an increase of the peak gain by 15%. For $T_L = 90$ K, see Fig. 2(b), the gain gets somewhat broadened and lowered in agreement with experiment;^{11,19} also here, ignoring the exchange effect or parallel spin collisions has similar effects on the simulated gain profile as discussed for $T_L = 10$ K.

In Fig. 3, the relative occupations and the electron temperatures are shown at $T_L = 10$ K for the eight energy levels within a miniband, characterized by their corresponding eigenenergies (compare Fig. 1(a)). The electron temperatures are extracted from the (generally non-thermal) carrier distributions in each subband by a least square fit. While the subband occupations do not depend much on the implementation of the exchange effect, the electron temperatures show a stronger dependence. For example, the extracted temperature for the 8th level (at 39.3 meV) varies from 121.6 K to 146.7 K, depending on the implementation of the spin dependence. The relative insensitivity of the population and the strong dependence of the electron temperature and gain on the implementation can be understood by looking at the average dwell time of an electron in a given subband, which is the inverse of the outscattering rate from this subband. In Fig. 4, the dwell time is shown for the eight energy levels, again characterized by their eigenenergies. The scattering is lowest, i.e., the dwell time is highest, when parallel spin collisions are ignored in the simulation (dashed curve). This is consistent with the reduced bandwidth and enhanced peak value of the corresponding gain

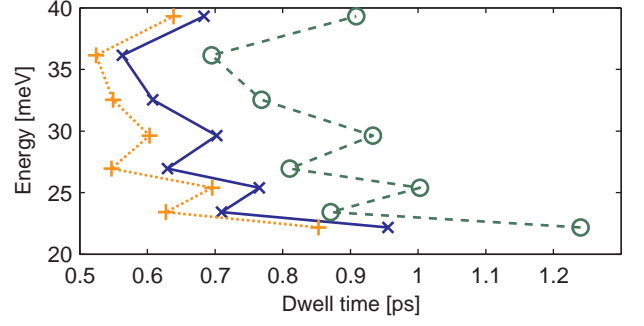


FIG. 4. (Color online) Simulation results for electron dwell times, as obtained by fully taking into account (x-marks, solid curves) and ignoring the exchange effect (plus signs, dotted curves), and by ignoring parallel spin collisions (circles, dashed curves). The lines are guide to the eye.

profile in Fig. 2(a), which are directly related to the outscattering rate.¹¹ On the other hand, the electron dwell time increases by a similar factor for all the subbands, thus explaining the relative insensitivity of subband occupations to the chosen implementation of Eq. (6).

C. Screening

Due to the computational effort involved in the RPA, screening is commonly taken into account using simplified models rather than solving Eq. (4) directly. The screening can for instance be considered by introducing a screening wavenumber q_s in Eq. (3), i.e., replacing the prefactor $e^2 / (2\epsilon Q)$ by $e^2 / [2\epsilon(Q + q_s)]$. In single subband models, q_s is obtained from Eq. (4) by assuming that screening is caused only by a single subband, e.g., the ground state.^{6,7} A modified approach, which has been shown to yield improved results for RP structures, is the modified single subband model⁷ with

$$q_s = \frac{e^2 m^*}{2\epsilon \pi \hbar^2} \sum_i f_i(\mathbf{k} = \mathbf{0}), \quad (8)$$

where i sums over the subbands in one period.

In Fig. 5, the intrasubband Coulomb matrix elements V_{1111} (Fig. 5(a)) and V_{1212} (Fig. 5(b)), as well as the intersubband element V_{1122} (Fig. 5(c)) are shown as a function of the wavenumber Q . Here, 1 and 2 denote the upper laser level at 22.2 meV and the level directly above at 23.4 meV, see Fig. 1(a). Displayed are the screened matrix elements based on the RPA (solid lines) and the simplified model according to Eq. (8) with $q_s = 0.0237 \text{ nm}^{-1}$ (dashed lines), as well as the bare matrix elements defined in Eq. (3) (dotted lines). As can be seen from Fig. 5(c), in the simplified screening model the intersubband elements approach zero for small wavenumbers, in contrast to the exact implementation of the RPA. A better approach consists in applying the simplified screening model only to the intrasubband matrix elements, and to treat intersubband scattering as unscreened.²²

Figure 6 contains the self-self-consistently simulated gain spectra at $T_L = 10$ K and $T_L = 90$ K. In contrast to Fig. 2,

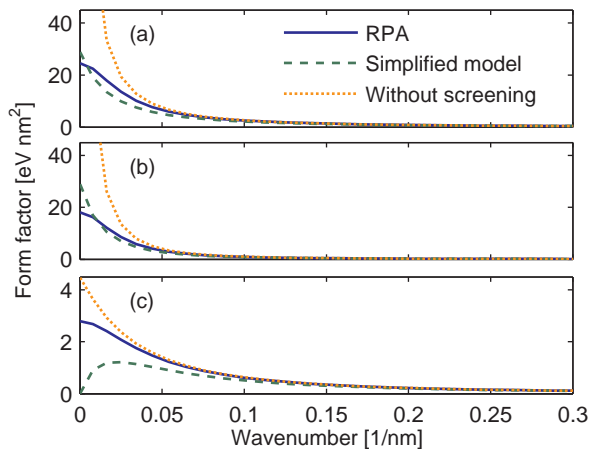


FIG. 5. (Color online) Screened and unscreened Coulomb matrix elements for the structure shown in Fig. 1(a). (a) V_{1111} ; (b) V_{1212} ; (c) V_{1122} .

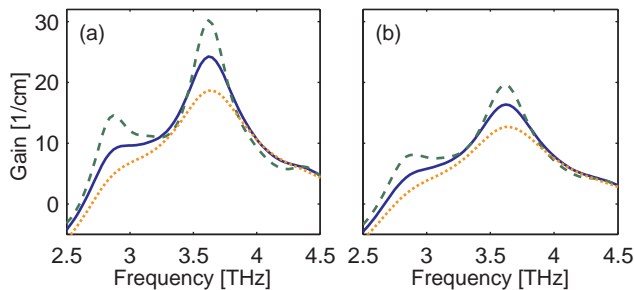


FIG. 6. (Color online) Simulated spectral gain vs frequency, as obtained by taking into account screening in the RPA (solid curves), and using the modified single subband model for all matrix elements (dashed curves) or for the intrasubband elements only (dotted curves), i.e., treating intersubband elements as unscreened. (a) $T_L = 10\text{K}$; (b) $T_L = 90\text{K}$.

the exchange effect is included, but different screening models are used. The reference curve based on the exact evaluation of the RPA (solid curves) agrees well with experiment, see Section III A. Applying the simplified screening model to all matrix elements overestimates the screening of the intersubband elements, compare Fig. 5(c), and thus results in an underestimation of scattering. The resulting spectral gain profile at 10 K (dashed curve in Fig. 6(a)) features a 25% enhanced gain peak and an excessively narrow FWHM width of 0.43 THz, as compared to an experimental value of 0.85 THz. On the other hand, completely ignoring the screening effect for the intersubband matrix elements overestimates the intersubband scattering, thus resulting in a lowered and broadened gain profile (dotted curves). As can be seen from Fig. 6(b), the simulation results at $T_L = 90\text{K}$ are affected in a similar way by using above discussed approximations. In Fig. 7, the obtained relative subband occupations and electron temperatures are compared at $T_L = 10\text{K}$ for the different implementations of screening. Although the simulated gain in Fig. 6 greatly depends on the applied screening model, the occupa-

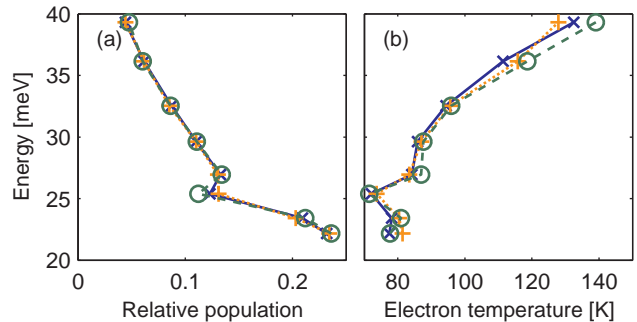


FIG. 7. (Color online) Simulation results for (a) relative subband occupations and (b) subband temperatures, as obtained by taking into account screening in the RPA (x-marks, solid curves), and using the modified single subband model for all matrix elements (circles, dashed curves) or for the intrasubband elements only (plus signs, dotted curves). The lines are guide to the eye.

tions of the miniband levels in Fig. 7(a) are quite insensitive to the chosen implementation, similarly as in Fig. 3. This is again consistent with the fact that the average dwell time of an electron in a level, shown in Fig. 8, strongly depends on the chosen screening model, but is changed by a similar factor for all subbands. We attribute this to the quasi-continuous nature of the minibands in the BTC structure. Contrariwise, for RP QCLs, where the energetic separation of the levels greatly varies, simple approaches like the single subband screening model have been shown to considerably affect the simulation results for the level occupations.^{6,7} Here, only a single subband, typically the ground level, is considered.⁷ However, it should be mentioned that also for the investigated BTC structure, this approach would yield somewhat less accurate results than evaluating Eq. (8), as done in our simulations. The kinetic electron distribution within each subband, represented by fitted electron temperatures in Fig. 7(b), shows a moderate dependence on the screening model. For example, the extracted temperatures in the 8th level (at 39.3 meV) ranges between 127.9 K and 139.0 K for the different screening models. Here again, more significant deviations from the RPA result would be obtained by using a single subband screening model rather than Eq. (8).

IV. CONCLUSIONS

Employing an EMC analysis, we have investigated the role of Coulomb interactions in THz BTC structures, and assessed the validity of common approximations for modeling Coulomb effects. We have shown that space charge effects lead to considerable conduction band bending, having a significant influence on the obtained wave functions and the energy level alignment. These mechanisms are properly accounted for in a self-self-consistent approach, i.e., by iteratively performing SP and EMC simulations until mutual convergence is achieved. Ignoring these effects leads to excessively lowered and broadened gain profiles, in sharp contradiction to experimental results. Also e-e scattering between

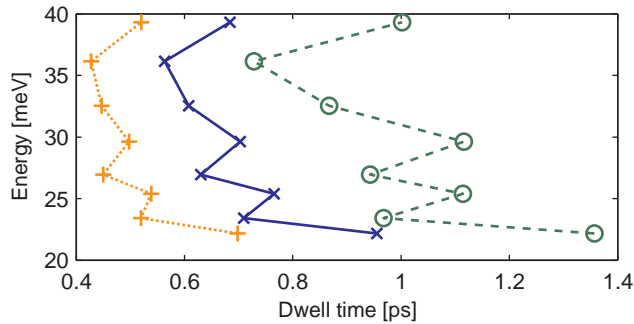


FIG. 8. (Color online) Simulation results for electron dwell times, as obtained by taking into account screening in the RPA (x-marks, solid curves), and using the modified single subband model for all matrix elements (circles, dashed curves) or for the intrasubband elements only (plus signs, dotted curves). The lines are guide to the eye.

the closely spaced miniband levels plays an important role for the carrier transport and the spectral gain profile. Common approximations in implementing e-e scattering, like neglecting the spin-related exchange effect or using simplified screening models, results in considerable deviations for the obtained gain profile. Even refined approximations, like the modified single subband screening model, introduce an error of approximately 25% for the peak gain in the investigated structure, as compared to simulations based on the full RPA. Combined with ignoring the spin dependence, the deviation can easily exceed 30%. With space charge effects and e-e scattering properly accounted for, the EMC analysis is shown to yield meaningful results for the investigated BTC design, which are found to be in good agreement with experiment.

ACKNOWLEDGMENTS

C.J. and A.M. acknowledge support from the Emmy Noether program of the German Research Foundation Grant No. DFG, JI115/1-1.

- ¹V. D. Jovanović, D. Indjin, N. Vukmirović, Z. Ikonić, P. Harrison, E. H. Linfield, H. Page, X. Marcadet, C. Sirtori, C. Worrall, H. E. Beere, and D. A. Ritchie, *Appl. Phys. Lett.* **86**, 211117 (2005).
- ²T. Kubis, C. Yeh, P. Vogl, A. Benz, G. Fasching, and C. Deutsch, *Phys. Rev. B* **79**, 195323 (2009).
- ³R. C. Iotti and F. Rossi, *Appl. Phys. Lett.* **78**, 2902 (2001).
- ⁴H. Callebaut, S. Kumar, B. S. Williams, Q. Hu, and J. L. Reno, *Appl. Phys. Lett.* **83**, 207 (2003).
- ⁵H. Callebaut, S. Kumar, B. S. Williams, Q. Hu, and J. L. Reno, *Appl. Phys. Lett.* **84**, 645 (2004).
- ⁶O. Bonno, J.-L. Thobel, and F. Dessenne, *J. Appl. Phys.* **97**, 043702 (2005).
- ⁷J. T. Lü and J. C. Cao, *Appl. Phys. Lett.* **89**, 211115 (2006).
- ⁸C. Jirauschek, G. Scarpa, P. Lugli, M. S. Vitiello, and G. Scamarcio, *J. Appl. Phys.* **101**, 086109 (2007).
- ⁹C. Jirauschek and P. Lugli, *Phys. Status Solidi C* **5**, 221 (2008).
- ¹⁰R. Köhler, R. C. Iotti, A. Tredicucci, and F. Rossi, *Appl. Phys. Lett.* **79**, 3920 (2001).
- ¹¹C. Jirauschek and P. Lugli, *J. Appl. Phys.* **105**, 123102 (2009).
- ¹²J. T. Lü and J. C. Cao, *Appl. Phys. Lett.* **88**, 061119 (2006).
- ¹³P. Lugli and D. K. Ferry, *IEEE Trans. Electron Devices* **32**, 2431 (1985).
- ¹⁴C. Jirauschek, *IEEE J. Quantum Electron.* **45**, 1059 (2009).
- ¹⁵S. M. Goodnick and P. Lugli, *Phys. Rev. B* **37**, 2578 (1988).
- ¹⁶M. Moško, A. Mošková, and V. Cambel, *Phys. Rev. B* **51**, 16860 (1995).
- ¹⁷S.-C. Lee and I. Galbraith, *Phys. Rev. B* **59**, 15796 (1999).
- ¹⁸M. Moško and A. Mošková, *Semicond. Sci. Technol.* **9**, 478 (1994).
- ¹⁹G. Scalari, L. Ajili, J. Faist, H. Beere, E. Linfield, D. Ritchie, and G. Davies, *Appl. Phys. Lett.* **82**, 3165 (2003).
- ²⁰A. Leuliet, A. Vasanelli, A. Wade, G. Fedorov, D. Smirnov, G. Bastard, and C. Sirtori, *Phys. Rev. B* **73**, 085311 (2006).
- ²¹R. Nelander and A. Wacker, *Appl. Phys. Lett.* **92**, 081102 (2008).
- ²²X. Gao, D. Botez, and I. Knezevic, *J. Appl. Phys.* **101**, 063101 (2007).